Sparse Blind Deconvolution of Ground Penetrating Radar Data

Sajad Jazayeri, Nasser Kazemi, and Sarah Kruse

***Abstract*— We propose an effective method for sparse blind deconvolution (SBD) of ground penetrating radar data. The SBD algorithm has no constraints on the phase of the wavelet, but the initial wavelet must be carefully captured from the data. The data are considered a convolution product of an unknown source wavelet and unknown sparse reflectivity series. The algorithm developed here is an alternating minimization technique that updates the reflectivity series and the wavelet iteratively. The reflectivity update is solved as an $\ell_2 - \ell_1$ problem with the alternating split Bregman iteration technique. The wavelet update is solved as an $\ell_2 - \ell_2$ problem with Wiener deconvolution. The algorithm converges to a local minimum. In order to increase the likelihood so that convergence coincides with the desired local minimum, special steps are taken to provide a proper initial wavelet. Synthetic and real data examples show that both subsurface reflectivity series and wavelet (amplitude and phase) can be estimated efficiently. The SBD method presented appears robust and compares favorably to previous studies in its resistance to noise.**

***Index Terms*— Deconvolution, ground penetrating radar (GPR), reflectivity, source wavelet, sparsity.**

I. Introduction

DECONVOLUTION is a popular deblurring technique used in signal and image processing, with applications in photography, remote sensing, astronomy, medical imaging, geophysics, and more [1], [2]. When successfully applied to blurry or distorted matrices, the result is a clearer image with more details. In geophysics, particularly in exploration seismology, the goal of deconvolution is higher resolution subsurface images [3]. Deconvolution works by removing the signature of the propagated waveform. Ideally, what is left is a representation of the subsurface pattern of reflection coefficients, which present a high-resolution subsurface image [4].

Deconvolution of ground penetrating radar (GPR) data is used to estimate the reflectivity series [5]–[13], to produce a higher resolution subsurface image or a clean reflectivity series that can be used for ray-based travel-time analysis. GPR deconvolution is also used to extract the shape of the transmitted pulse [14]–[16], for use in modeling procedures such as full-waveform inversion (FWI). Factors such as antenna-ground coupling and Earth's filtering effects due to soil's characteristics alter the shape of the wavelet [10], which make it challenging to estimate the waveform and reflectivity series.

The widely used Wiener deconvolution [17], [18] has some disadvantages when applied to GPR data. Wiener deconvolution assumes that the reflectivity series has an ideal statistical property, i.e., it is white noise, and the wavelet has a minimum phase characteristics [17], [18]. However, Ricker [19] shows that due to the earth filtering, the average wavelet is different from the near-source signature. We show, here, that when using the Wiener deconvolution method, we can only estimate a smooth reflectivity series and a residual wavelet; any difference between the actual wavelet and its minimum phase equivalent remains untouched in the recovered reflectivity series. Fortunately, a body of literature shows the possibility of estimating nonminimum phase wavelets by imposing a sparsity constraint instead of a white noise assumption (i.e., Gaussian distribution) on the reflectivity series [20]–[25].

The alternative deconvolution method is referred to as sparse blind deconvolution (SBD). A sparsity assumption is imposed on the matrix of reflection coefficients. The process begins "blindly" in that it is formulated to start without requiring a starting model of reflection coefficients, or without a starting model for the source wavelet. The sparsity assumption is well adapted to enhancing the resolution of thin layers and isolated buried objects. The method thus holds promise particularly for both layered geological features and engineering, archeological, or tree root applications where finite objects produce distinctive returns within a background of soil structure. Few studies have applied a sparsity assumption while performing deconvolution on GPR data [26], [27]. The method presented by Chahine *et al.* [26] improves image resolution in the presence of thin layers by sparsity maximization in the reflectivity series with results similar to spiking deconvolution. Their method requires a minimum phase wavelet and is sensitive to noise. Li [27] introduces an alternating iterative method to solve the nonconvex optimization problem, with a threshold maximum for the reflector amplitudes to avoid trapping the solution in local minima. Tested only on synthetic data, Li's algorithm struggles to recover the shape and the phase of the source wavelet in the presence of noise.

In this paper, we propose an alternating SBD method targeting GPR data, which may be more robust in the presence of noise. The algorithm estimates both the wavelet and the

Manuscript received April 27, 2018; revised August 10, 2018 and September 23, 2018; accepted November 18, 2018. *(Corresponding author: Sajad Jazayeri.)*

S. Jazayeri and S. Kruse are with the School of Geosciences, University of South Florida, Tampa, FL 33620 USA (e-mail: sjazayeri@mail.usf.edu; skruse@usf.edu).

N. Kazemi is with the Department of Chemical and Petroleum Engineering, University of Calgary, Calgary, AB T2N 1N4, Canada (e-mail: nasser.kazeminojadeh@ucalgary.ca).

Digital Object Identifier 10.1109/TGRS.2018.2886741

reflectivity series iteratively while removing any constraints on the phase of the wavelet. The optimization problem in this paper is nonlinear when we consider both reflectivity series and the wavelet as unknowns. However, if we fix the wavelet, the cost function will be linear with regards to the reflectivity series and vice versa. There are nonlinear algorithms that aim at finding the global solution of the original problem; however, nonlinear algorithms are computationally expensive. Instead, we solve the cost function in an alternating fashion, which allows us to use fast and efficient solvers. The drawback is that the algorithm is a local minimization technique and, therefore, requires a proper initial model. To remedy this shortcoming, we carefully capture an initial wavelet estimate from the data (this initial estimate is improved upon in the optimization process). The selection of parameters required for the inversion is automated. The blind recovery of the reflectivity series and wavelet is found to be stable on a range of synthetic and field data scenarios. The examples selected to show in this paper focus on distinct cylindrical sources, such as pipes and roots, in a soil background. In these scenarios, the proposed method provides a higher resolution reflectivity series than Wiener deconvolution and appears to be more stable in the presence of noise.

We begin this paper with the larger context for this paper, introducing convolution, deconvolution, and blind deconvolution models. Within this framework, our method is detailed and then tested on both synthetic and field data.

A. Convolution Model

The impulse response of the earth can be modeled as a linear time-invariant system [28]. In geophysics, the impulse response is called the reflectivity series. Assuming a stationary blurring kernel, the recorded GPR data at the surface are defined as the convolution of the blurring kernel with the impulse response of the earth. The blurring kernel refers to an imperfection of the system (low-pass filter), which results in lowering the resolution of the recorded data. If we assume that the blurring kernel does not change through time, it is called a stationary blurring kernel. In different fields of study, this imperfection is defined as the blurring kernel, source signature, source wavelet, point spread function, wavelet, and so on. In the geophysics community, this low-pass filter comes from the source wavelet which is band-limited, and when it is convolved with the reflectivity series, it lowers the resolution of the data. In this paper, we will call this blurring kernel the source wavelet or wavelet for short. The input–output relationship for this system can be written as follows:

$$d_j[n] = \sum_k w[n-k] r_j[k] + e_j[n], \quad j = 1, 2, \ldots J \tag{1}$$

where the GPR data in the trace j are given by $\mathbf{d}_j = (d_j[0], d_j[1], \ldots, d_j[N-1])^T$. Similarly, the impulse response for trace j is given by $\mathbf{r}_j = (r_j[0], r_j[1], \ldots, r_j[M-1])^T$, $\mathbf{e}_j = (e_j[0], e_j[1], \ldots, e_j[N-1])^T$ is the additive noise term, and the stationary GPR wavelet is $\mathbf{w} = (w[0], w[1], \ldots, w[L-1])^T$, and T stands for transpose operator. We stress that $N = M + L - 1$. In matrix vector notation, (1) can be cast as

$$\mathbf{d}_j = \mathbf{W}\,\mathbf{r}_j + \mathbf{e}_j\,, \quad j = 1, 2, \ldots J \tag{2}$$

where $\mathbf{W}$ is the convolution matrix built from the wavelet. To be more specific, the matrix $\mathbf{W}$ has a Toeplitz structure with entries

$$\mathbf{W} = \begin{pmatrix} w(0) & & & & & \\ w(1) & w(0) & & & & \\ w(2) & w(1) & w(0) & & & \\ \vdots & & & \ddots & & \\ & & & w(L-1) & w(L-2) & \\ & & & & w(L-1) & \end{pmatrix}. \tag{3}$$

We would also like to remind the readers that using commutative property of convolution, (2) is equivalent to

$$\mathbf{d}_j = \mathbf{R}_j\,\mathbf{w} + \mathbf{e}_j, \quad j = 1, 2, \ldots J \tag{4}$$

where $\mathbf{R}_j$ is the convolution matrix built from the reflectivity series of channel j with proper dimensions.

B. Deconvolution Model

1) Deconvolution to Estimate the Reflectivities: Deterministic deconvolution can be used to remove the effect of the wavelet from the data if the wavelet is known. In some rare cases, the signature of the source is known, as, for example, if the source is fully controlled. In other cases, the wavelet can be estimated from the data. This is done, for example, in marine seismic by averaging the signature of the ocean bottom reflector [29]. Assuming that the wavelet is known *a priori*, the idea is to design a filter $\mathbf{f}_w$ such that when applied to the data, the output would represent the reflectivity series

$$\mathbf{r} = \mathbf{F}_w \mathbf{d} \tag{5}$$

where $\mathbf{d} = [\mathbf{d}_1^T, \mathbf{d}_2^T, \ldots, \mathbf{d}_N^T]^T$, $\mathbf{F}_w$ is the convolution matrix built from $\mathbf{f}_w$, and $\mathbf{r} = [\mathbf{r}_1^T, \mathbf{r}_2^T, \ldots, \mathbf{r}_J^T]^T$ is the estimated reflectivity series. Ideally, $\mathbf{F}_w$ should be the inverse of $\mathbf{H}$ where $\mathbf{H}$ is a block diagonal matrix with J blocks each block being equal to $\mathbf{W}$. Unfortunately, the $\mathbf{H}$ matrix is not invertible. The simplest solution for inverting the $\mathbf{H}$ matrix is the Wiener deconvolution method, which is the solution to

$$\mathbf{r} = \underset{\mathbf{r}}{\operatorname{argmin}} \, ||\mathbf{H}\mathbf{r} - \mathbf{d}||_2^2. \tag{6}$$

Equation (6) is a convex optimization problem and has a closed-form solution

$$\mathbf{r} = (\mathbf{H}^T\mathbf{H})^{-1}\mathbf{H}^T\mathbf{d}. \tag{7}$$

Comparing (5) and (7) implies that $\mathbf{F}_w = (\mathbf{H}^T\mathbf{H})^{-1}\mathbf{H}^T$. To estimate a physically plausible reflectivity series, we could also incorporate more information about the reflectivity series into (6)

$$\mathbf{r} = \underset{\mathbf{r}}{\operatorname{argmin}} \, ||\mathbf{H}\mathbf{r} - \mathbf{d}||_2^2 + \lambda_r \mathcal{R}(\mathbf{r}) \tag{8}$$

where $\mathcal{R}(\mathbf{r})$ is a regularization term that enhances some desired features in the reflectivity series and λ_r is a regularization parameter that balances the importance of data fidelity and priori information about the reflectivity series.

2) Deconvolution to Estimate the Wavelet: In a process analogous to Section I-B.1, deterministic deconvolution can be used to remove the effect of the reflectivity series from the data, if the reflectivity series is known. This can be done at well locations, where well logs are used to generate the reflectivity series [30], [31]. The generated reflectivity series are then used to estimate the waveform. The result can serve as a global waveform for further types of modeling or as an input to an FWI workflow. In GPR, a well-known approach is to estimate the subsurface reflectivity series by performing ray-based inversion. The estimated reflectivity equivalent structure (which is used in the same manner as well data for seismic) is then deconvolved from the collected data to estimate the wavelet [14]–[16]. In this case, deconvolution simply is done by finding a filter $\mathbf{f}_r$ such that when applied to the data, the output would represent the wavelet

$$\mathbf{w} = \mathbf{F}_r \mathbf{d} \tag{9}$$

where $\mathbf{F}_r$ is the convolution matrix built from $\mathbf{f}_r$ and $\mathbf{w}$ is the estimated wavelet. Ideally, $\mathbf{F}_r$ should be the inverse of $\mathbf{R}$ where $\mathbf{R}$ is a matrix with entries

$$\mathbf{R} = \begin{pmatrix} \mathbf{R}_1 \\ \mathbf{R}_2 \\ \mathbf{R}_3 \\ \vdots \\ \mathbf{R}_{J-1} \\ \mathbf{R}_J \end{pmatrix}. \tag{10}$$

The $\mathbf{R}$ matrix is not invertible, so the simplest solution for inverting the matrix is the Wiener deconvolution method, which is the solution to

$$\mathbf{w} = \underset{\mathbf{w}}{\operatorname{argmin}} \, ||\mathbf{R}\mathbf{w} - \mathbf{d}||_2^2. \tag{11}$$

Equation (11) is a convex optimization problem and has a closed-form solution

$$\mathbf{w} = (\mathbf{R}^T\mathbf{R})^{-1}\mathbf{R}^T\mathbf{d}. \tag{12}$$

Comparing (9) and (12) implies that $\mathbf{F}_r = (\mathbf{R}^T\mathbf{R})^{-1}\mathbf{R}^T$. To estimate a physically plausible wavelet, we also incorporate more information about the wavelet into (11)

$$\mathbf{w} = \underset{\mathbf{w}}{\operatorname{argmin}} \, ||\mathbf{R}\mathbf{w} - \mathbf{d}||_2^2 + \lambda_w \mathcal{R}(\mathbf{w}) \tag{13}$$

where $\mathcal{R}(\mathbf{w})$ is a regularization term which enhances some desired features in the estimated wavelet and λ_w is a regularization parameter that balances the importance of data fidelity and the knowledge of the wavelet.

3) Blind Deconvolution: If neither the signature of the wavelet nor the subsurface reflectivity structure is known, the problem is a so-called blind deconvolution problem [23], [24], [32]. This is, of course, a common real-world scenario, and thus, there are many reasons that blind deconvolution solutions are desirable. Even when borehole data are used to build reflectivity series, large data gaps remain between boreholes, and the larger reflectivity structure is incompletely known. Ray-based inversion to obtain geometry of subsurface reflectors can be inaccurate since it uses only the first arrival times of the diffracted pulses, a very small portion of the total recorded signal. The ray-based inversion process itself can be time-consuming. Finally, errors in the ray-based results (or any reflectivity structure) will harm estimates of the wavelet. In the real world, the signature of a GPR wavelet is generally unknown and affected not only by the instrument but also by coupling between antenna and soil, and soil electrical characteristics that are, in turn, influenced by soil moisture content. For FWI, which better uses the total recorded signal, knowledge of the wavelet becomes extremely important. Any error in the phase or the amplitude of the wavelet propagates into the FWI subsurface characterization. To address this common scenario, namely, lack of *a priori* knowledge about both the wavelet and subsurface reflectivity structure, blind deconvolution formulates the problem in such a way that it simultaneously solves for the wavelet and the reflectivity series.

The general cost function in our blind deconvolution problem is defined as

$$\{\mathbf{w}, \mathbf{r}\} = \underset{\mathbf{w},\mathbf{r}}{\operatorname{argmin}} \, ||\mathbf{H}\mathbf{r} - \mathbf{d}||_p^p + \lambda_r \mathcal{R}(\mathbf{r}) + \lambda_w \mathcal{R}(\mathbf{w}) \tag{14}$$

where $p > 0$, $\lambda_w, \lambda_r > 0$, $\|\mathbf{a}\|_p^p = \sum_{i=1}^N |a_i|^p$ with $\mathbf{a} = [a_1, a_2, \ldots, a_{N-1}, a_N]^T$, and $\|\mathbf{H}\mathbf{r} - \mathbf{d}\|_p^p$ is a closed convex function.

C. Problem Statement and the Proposed Approach

In this writeup, we assume that an added noise term in the data has a Gaussian distribution and the subsurface reflectivity series can be cast as a sparse series (i.e., few reflectors that in the GPR case could represent any anomaly that reflects energy). The sparse reflectivity assumption is valid for layered media and shows promising performance in the context of the deconvolution problem [2], [20], [23], [24], [33]. We also assume that the wavelet is a smooth function. After incorporating these assumptions into (14), we have

$$\{\mathbf{w}, \mathbf{r}\} = \underset{\mathbf{w},\mathbf{r}}{\operatorname{argmin}} \, ||\mathbf{H}\mathbf{r} - \mathbf{d}||_2^2 + \lambda_r ||\mathbf{r}||_1 + \lambda_w ||\mathbf{w}||_2^2 \tag{15}$$

and we remind the reader that (15) is equal to

$$\{\mathbf{w}, \mathbf{r}\} = \underset{\mathbf{w},\mathbf{r}}{\operatorname{argmin}} \, ||\mathbf{R}\mathbf{w} - \mathbf{d}||_2^2 + \lambda_r ||\mathbf{r}||_1 + \lambda_w ||\mathbf{w}||_2^2. \tag{16}$$

Equation (15) is solved with an alternating minimization technique. First, we solve for reflectivity series by fixing the wavelet, simplifying (15) to

$$\mathbf{r} = \underset{\mathbf{r}}{\operatorname{argmin}} \, ||\mathbf{H}\mathbf{r} - \mathbf{d}||_2^2 + \lambda_r ||\mathbf{r}||_1 \tag{17}$$

which is an $\ell_2 - \ell_1$ problem and can be solved with any $\ell_2 - \ell_1$ solvers, such as unconstrained basis pursuit denoising (UBPDN) via alternating split Bregman algorithms [2], [34], [35], Euclid in a Taxicab ℓ_1/ℓ_2 regularization [36], majorization-minimization optimization [37], alternating minimization [1], and gradient projection [38]. In this paper, we use the UBPDN solved with the alternating split Bregman algorithm to estimate the sparse reflectivity structure.

The next step is to estimate the wavelet by fixing the reflectivity series. In this case, (15) or equivalently (16)

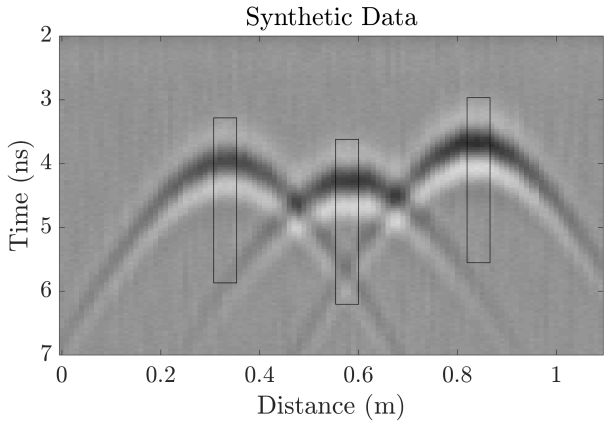

Fig. 1. Synthetic 1-GHz 3-D GPR model of a profile run perpendicular over three cylinders with 1.2-GHz noise and 500-MHz noise. Black boxes contain trace segments used for initial wavelet estimation. Traces are computed for 7 ns; the earliest portions of the traces containing the direct wave arrivals are removed from the analysis.

simplifies to

$$\mathbf{w} = \underset{\mathbf{w}}{\operatorname{argmin}} \, ||\mathbf{R}\mathbf{w} - \mathbf{d}||_2^2 + \lambda_w ||\mathbf{w}||_2^2 \tag{18}$$

which is an $\ell_2 - \ell_2$ problem and has a closed-form solution

$$\mathbf{w} = (\mathbf{R}^T\mathbf{R} + \lambda_w \mathbf{I})^{-1}\mathbf{R}^T\mathbf{d} \tag{19}$$

where $\mathbf{I}$ is the identity matrix.

At this point, we stress that the alternating minimization technique is a local minimization approach and special steps must be taken to initialize the unknown variables $\mathbf{w}$ and $\mathbf{r}$. The initial estimation of the wavelet is of particular importance and discussed further below.

II. Methodology

The proposed SBD method has two stages, the initialization and the main optimization. Our main optimization algorithm is an alternating minimization technique. Because we begin with (17) (updating the reflectivity with wavelet fixed), we require the formulation of an initial wavelet. The main algorithm then solves the general SBD equation (15) or (16) by defining the two subproblems for reflectivity and wavelet expressed in (17) and (18), respectively.

A. Algorithm Initialization

The proposed algorithm is a local minimizer and, therefore, sensitive to the initial wavelet. For the ground-coupled GPR scenarios considered here, the method is successful when we obtain the initial wavelet from the data. To estimate the initial wavelet, windowed portions of several traces near the apex of the hyperbolic events in the data are averaged, as shown, for example, in the black squared windows in Fig. 1. The windowed traces are first shifted relative to one another to maximize the zero-lag cross correlation. Then, the shifted traces are stacked and normalized to provide the initial wavelet. We note the initial wavelet is estimated in this fashion from the data in both synthetic and real data examples.

B. Main Optimization

This section describes the alternating minimization technique. First, we illustrate updating the reflectivity series by the alternating split Bregman algorithm for solving (17) and then updating the wavelet by solving (19).

1) Updating Reflectivity With the Alternating Split Bregman Algorithm: Bregman iteration regularization is based on the Bregman distance and solves a constrained optimization problem with a general form of

$$\mathbf{r} = \underset{\mathbf{r}}{\operatorname{argmin}} \, \mathcal{C}_1(\mathbf{r}) \quad \text{s.t. } \mathcal{C}_2(\mathbf{r}) = 0 \tag{20}$$

with $\mathcal{C}_1$ and $\mathcal{C}_2$ convex, $\mathcal{C}_2$ differentiable, and $\operatorname{argmin}_{\mathbf{r}} \mathcal{C}_2(\mathbf{r}) = 0$. The Bregman distance of functional $\mathcal{C}_1$ between two points $\mathbf{r}_1$ and $\mathbf{r}_2$ is defined as

$$BD^{\mathbf{g}}_{\mathcal{C}_1}(\mathbf{r}_1, \mathbf{r}_2) = \mathcal{C}_1(\mathbf{r}_1) - \mathcal{C}_1(\mathbf{r}_2) - \langle \mathbf{g}, \mathbf{r}_1 - \mathbf{r}_2 \rangle \tag{21}$$

where $\mathbf{g} \in \partial\mathcal{C}_1(\mathbf{r}_2)$ is a subgradient of $\mathcal{C}_1$ at the $\mathbf{r}_2$ point. Bregman iterative regularization solves the problem stated in (20) by a sequence of convex problems

$$\mathbf{r} = \underset{\mathbf{r}}{\operatorname{argmin}} \, \mathcal{C}_1(\mathbf{r}) - \langle \mathbf{g}^k, \mathbf{r} \rangle + \lambda \mathcal{C}_2(\mathbf{r}) \tag{22}$$

and

$$\mathbf{g}^{k+1} = \mathbf{g}^k - \lambda \nabla \mathcal{C}_2(\mathbf{r}^{k+1}) \tag{23}$$

with $k = 0, 1, 2, \ldots$ the iteration number, $\lambda > 0$, ∇ is the gradient operator, and $\mathbf{g}^{k+1} \in \partial\mathcal{C}_1(\mathbf{r}^{k+1})$. To take advantage of the Bregman iteration, we need to rewrite (17) with a similar format to that in (20)

$$\{\mathbf{r}, \mathbf{t}_1\} = \underset{\mathbf{r},\mathbf{t}_1}{\operatorname{argmin}} \, ||\mathbf{t}_1||_2^2 + \lambda_r ||\mathbf{r}||_1 \quad \text{s.t. } \mathbf{t}_1 - (\mathbf{H}\mathbf{r} - \mathbf{d}) = 0 \tag{24}$$

with $\mathbf{t}_1 = \mathbf{H}\mathbf{r} - \mathbf{d}$. Comparing (24) and (20) reveals that $\mathcal{C}_1(\mathbf{r}, \mathbf{t}_1) = ||\mathbf{t}_1||_2^2 + \lambda_r ||\mathbf{r}||_1$ and $\mathcal{C}_2(\mathbf{r}, \mathbf{t}_1) = \mathbf{t}_1 - (\mathbf{H}\mathbf{r} - \mathbf{d})$. Using the new $\mathcal{C}_1$ and $\mathcal{C}_2$ functionals and defining $\mathbf{t}_2 = \mathbf{r}$, we derive the simplified Bregman iterations (for detailed derivations see [39]) as

$$\begin{aligned}\{\mathbf{r}^{k+1}, \mathbf{t}_1{}^{k+1}, \mathbf{t}_2{}^{k+1}\} = \underset{\mathbf{r},\mathbf{t}_1,\mathbf{t}_2}{\operatorname{argmin}} \; & ||\mathbf{t}_1||_2^2 + \lambda_r ||\mathbf{t}_2||_1 \\ & + \frac{\alpha}{2}\left\|\mathbf{t}_1 - (\mathbf{H}\mathbf{r} - \mathbf{y}) - \mathbf{g}_1^k\right\| \\ & + \frac{\beta}{2}\left\|\mathbf{t}_2 - \mathbf{r} - \mathbf{g}_2^k\right\|_2^2 \end{aligned} \tag{25}$$

$$\mathbf{g}_1^{k+1} = \mathbf{g}_1^k - \left[\mathbf{t}_1^{k+1} - (\mathbf{H}\mathbf{r}^{k+1} - \mathbf{y})\right] \tag{26}$$

$$\mathbf{g}_2^{k+1} = \mathbf{g}_2^k - \left[\mathbf{t}_2^{k+1} - \mathbf{r}^{k+1}\right] \tag{27}$$

with $\mathbf{g}_1^0 = \mathbf{g}_2^0 = \mathbf{0}$ and $\alpha, \beta > 0$. The final step is to solve (25). Goldstein and Osher [39] show that (25) can be divided into three sub-problems where

$$\mathbf{r}^{k+1} = \underset{\mathbf{r}}{\operatorname{argmin}} \, \frac{\alpha}{2}\left\|\mathbf{t}_1^k - (\mathbf{H}\mathbf{r} - \mathbf{y}) - \mathbf{g}_1^k\right\| + \frac{\beta}{2}\left\|\mathbf{t}_2^k - \mathbf{r} - \mathbf{g}_2^k\right\|_2^2 \tag{28}$$

$$\mathbf{t}_1^{k+1} = \underset{\mathbf{d}}{\operatorname{argmin}} \, \frac{\alpha}{2}||\mathbf{d} - (\mathbf{H}\mathbf{r}^{k+1} - \mathbf{y}) - \mathbf{g}_1^k|| + ||\mathbf{d}||_2^2 \tag{29}$$

$$\mathbf{t}_2^{k+1} = \underset{\mathbf{d}}{\operatorname{argmin}} \, \frac{\beta}{2}\left\|\mathbf{d} - \mathbf{H}\mathbf{r}^{k+1} - \mathbf{g}_2^k\right\| + \lambda_r ||\mathbf{d}||_1. \tag{30}$$

Equations (28) and (29) have closed-form solutions

$$\mathbf{r}^{k+1} = \mathbf{P}^{-1}\left(\alpha \mathbf{H}^T\left[\mathbf{t}_1^k - \mathbf{g}_1^k + \mathbf{y}\right] + \beta\left[\mathbf{t}_2^k - \mathbf{g}_2^k\right]\right) \tag{31}$$

and

$$\mathbf{t}_1^{k+1} = \frac{\mathbf{H}\mathbf{r}^{k+1} - \mathbf{y} + \mathbf{g}_1^k}{1 + \frac{2}{\alpha}} \tag{32}$$

where $\mathbf{P} = \alpha \mathbf{H}^T\mathbf{H} + \beta \mathbf{I}$ and $\mathbf{I}$ is the identity matrix. Finally, in the case of (30), Goldstein and Osher argue that a single-iteration update is enough to approximate the solution. Accordingly, the single-iteration solution of (30) is defined as

$$\mathbf{t}_2^{k+1} = \text{prox}_{\frac{\lambda_r}{\beta}}\left(\mathbf{r}^{k+1} + \mathbf{g}_2^k\right) \tag{33}$$

where prox is a proximity operator and is defined as $\text{prox}_\tau(\mathbf{a}) = \text{sign}(\mathbf{a}) \odot \max(|\mathbf{a}| - \tau, 0)$ and $\odot$ is the Hadamard product. At this point by using (31)–(33) along with (26) and (27), we finalize the alternating split Bregman algorithm (Algorithm 1).

Algorithm 1 Alternating Split Bregman Algorithm as a Minimizer of 24 in the Time Domain

Require: $\mathbf{d}$, $\mathbf{H}$, λ_r, α, β
  Initialize: $k = 0, \mathbf{t}_1^0 = \mathbf{t}_2^0 = \mathbf{g}_1^0 = \mathbf{g}_1^0 = \mathbf{0}$
  while $\|\mathbf{r}^k - \mathbf{r}^{k-1}\|_2^2 > tol$ **do**
    $\mathbf{r}^{k+1} = \mathbf{P}^{-1}(\alpha \mathbf{H}^T[\mathbf{t}_1^k - \mathbf{g}_1^k + \mathbf{y}] + \beta[\mathbf{t}_2^k - \mathbf{g}_2^k])$
    $\mathbf{t}_1^{k+1} = \frac{\mathbf{H}\mathbf{r}^{k+1} - \mathbf{y} + \mathbf{g}_1^k}{1+\frac{2}{\alpha}}$
    $\mathbf{t}_2^{k+1} = prox_{\frac{\lambda_r}{\beta}}(\mathbf{r}^{k+1} + \mathbf{g}_2^k)$
    $\mathbf{g}_1^{k+1} = \mathbf{g}_1^k - [\mathbf{t}_1^{k+1} - (\mathbf{H}\mathbf{r}^{k+1} - \mathbf{y})]$
    $\mathbf{g}_2^{k+1} = \mathbf{g}_2^k - [\mathbf{t}_2^{k+1} - \mathbf{r}^{k+1}]$
    $k \leftarrow k + 1$
  end while
  return $\mathbf{r} = \mathbf{r}^k$

Algorithm 1 can efficiently solve (24). However, close inspection of the algorithm shows the matrix $\mathbf{P}$ has a block diagonal structure with each block being a Toeplitz matrix that can be diagonalized in the frequency domain. Accordingly, the update of $\mathbf{r}^{k+1}$ step can be formulated as a Wiener deconvolution in the frequency domain without any direct inversion of the $\mathbf{P}$ matrix. Hence, we formulate the alternating split Bregman algorithm in the frequency domain to decrease the computational cost of the algorithm. To do so, the Fourier equivalent of variables is defined as $\hat{\mathbf{w}} = \mathcal{F}\mathbf{w}$, $\hat{\mathbf{r}} = \mathcal{F}\mathbf{r}$, where $\mathcal{F}$ is a Fourier transform operator with $\mathcal{F}_{m,n} = \exp(-i2\pi mn/N)$, $i = \sqrt{-1}$, $m, n = 0, 1, 2, \ldots, N-1$, and the inverse Fourier transform is $\mathcal{F}^{-1} = (1/N)\mathcal{F}^*$, where $*$ indicates the complex conjugate. Using these Fourier pairs, we can write $\mathbf{H} = \mathcal{F}^{-1}\mathbf{H}_f\mathcal{F}$ where $\mathbf{H}_f$ is a diagonal matrix with J matrices built from $\text{diag}(\hat{\mathbf{w}})$ where $\text{diag}(\cdot)$ reshapes the vector to a diagonal matrix. Now, we have all the ingredients to formulate the alternating split Bregman algorithm in the frequency domain (Algorithm 2).

2) Updating the Wavelet: To update the wavelet, we need to solve (18), which has the closed-form solution shown in (19). Equation (19) can also be solved in the frequency domain since the matrix $\mathbf{R}$ has a Toeplitz structure and can be diagonalized in the frequency domain

$$\mathbf{w} = \mathcal{F}^{-1}\left[\frac{\sum_{j=1}^J \hat{\mathbf{r}}_j^* \odot \hat{\mathbf{d}}_j}{\bar{\mathbf{r}} + \lambda_w}\right] \tag{34}$$

where $\bar{\mathbf{r}} = \sum_{j=1}^J \hat{\mathbf{r}}_j^* \odot \hat{\mathbf{r}}_j$, $\odot$ is the Hadamard product, and $\hat{\mathbf{r}}_j$ and $\hat{\mathbf{d}}_j$ are the Fourier pairs of reflectivity and data in trace j, respectively.

Algorithm 2 Alternating Split Bregman Algorithm as a Minimizer of 24 in the Frequency Domain

Require: $\mathbf{d}$, $\mathbf{H}_f$, $\hat{\mathbf{w}}$, λ_r, α, β
  Define: $\mathbf{D} = diag(\frac{1}{(\alpha|\hat{\mathbf{w}}|^2+\beta)})$
  Initialize: $k = 0, \mathbf{t}_1^0 = \mathbf{t}_2^0 = \mathbf{g}_1^0 = \mathbf{g}_1^0 = \mathbf{0}$
  while $\|\hat{\mathbf{r}}^k - \hat{\mathbf{r}}^{k-1}\|_2^2 > tol$ **do**
    $\hat{\mathbf{r}}^{k+1} = \mathbf{D}(\alpha \mathbf{H}_f^* \mathcal{F}[\mathbf{t}_1^k - \mathbf{g}_1^k + \mathbf{y}] + \beta \mathcal{F}[\mathbf{t}_2^k - \mathbf{g}_2^k])$
    $\mathbf{t}_1^{k+1} = \frac{\mathcal{F}^{-1}\mathbf{H}_f\hat{\mathbf{r}}^{k+1} - \mathbf{y} + \mathbf{g}_1^k}{1+\frac{2}{\alpha}}$
    $\mathbf{t}_2^{k+1} = prox_{\frac{\lambda_r}{\beta}}(\mathcal{F}^{-1}\hat{\mathbf{r}}^{k+1} + \mathbf{g}_2^k)$
    $\mathbf{g}_1^{k+1} = \mathbf{g}_1^k - [\mathbf{t}_1^{k+1} - (\mathcal{F}^{-1}\mathbf{H}_f\hat{\mathbf{r}}^{k+1} - \mathbf{y})]$
    $\mathbf{g}_2^{k+1} = \mathbf{g}_2^k - [\mathbf{t}_2^{k+1} - \mathcal{F}^{-1}\hat{\mathbf{r}}^{k+1}]$
    $k \leftarrow k + 1$
  end while
  return $\mathbf{r} = \mathbf{t}_2^k$

C. SBD Algorithm

After defining the initialization step and the main optimization workflow for updating the reflectivity series and the wavelet, we can finalize the SBD algorithm. We use the more efficient frequency domain methods. Algorithm 3 shows the steps.

Algorithm 3 SBD Algorithm

Require: $\mathbf{d}$, L, λ_r, λ_w, α, β
  Define initial wavelet [using Algorithm initialization]: $\mathbf{w}^0$
  k=0
  while $\|\mathbf{H}\mathbf{r} - \mathbf{d}\|_2^2 > tol$ **do**
    Update $\mathbf{H}^k$ *using* $\mathbf{w}^k$
    Update reflectivity [using Algorithm 2]
    $\mathbf{r}^{k+1} = \underset{\mathbf{r}}{\text{argmin}}\ ||\mathbf{H}^k\mathbf{r} - \mathbf{d}||_2^2 + \lambda_r||\mathbf{r}||_1$
    Update $\mathbf{R}^{k+1}$ *using* $\mathbf{r}^{k+1}$
    Update wavelet [using (34)]
    $\mathbf{w}^{k+1} = \underset{\mathbf{w}}{\text{argmin}}\ ||\mathbf{R}^{k+1}\mathbf{w} - \mathbf{d}||_2^2 + \lambda_w||\mathbf{w}||_2^2$
    $k \leftarrow k + 1$
  end while
  return $\mathbf{r} \leftarrow \mathbf{r}^k$, $\mathbf{w} \leftarrow \mathbf{w}^k$

III. Parameter Selection

In this section, we describe our parameter selection strategies. The main parameters are length of wavelet L, regularization parameter for reflectivity update λ_r, and regularization

parameter for wavelet update λ_w. The length of the wavelet, L, is defined subjectively as a full wavelength, which may include a "tail" over which the pulse amplitudes converge to zero (examples are shown in results below).

The choice of regularization parameter λ_r has a significant impact on the estimated reflectivities. If the noise level δ is known, Pareto curves can be used to define λ_r [40], [41]. Alternatively, the minimizer of the generalized cross-validation (GCV) score [42] can be used for selecting the regularization parameter

$$\mathrm{GCV}(\lambda_r) = \frac{\|\mathbf{H}\ \mathbf{r}_{\lambda_\mathbf{r}} - \mathbf{d}\|_2^2}{(N - C \times \|\mathbf{r}_{\lambda_r}\|_0)^2} \tag{35}$$

where $\|\cdot\|_0$ is an ℓ_0 norm that counts the number of nonzero elements, C is an stabilizing parameter [43], and $\mathbf{r}_{\lambda_r}$ is the solution of (17) to a specific regularization parameter λ_r. A range of different parameters are tested and the minimizer of the GCV score is selected as the optimum λ_r. The GCV score method has the advantage of not requiring any prior information about the noise level so is used for real-data cases. Our tests on synthetic data show that the λ_r values estimated from the Pareto curve and the GCV score are similar.

For the wavelet update, we need to define the optimum λ_w parameter. Again, we make use of GCV score. The score for the Wiener deconvolution formulation of the wavelet estimation [2], [44] is defined as

$$\mathrm{GCV}(\lambda_w) = \frac{\|\mathbf{R}\ \mathbf{w}_{\lambda_\mathbf{w}} - \mathbf{d}\|_2^2}{\left(N - C \times \sum_{k=0}^{N-1} \frac{|\hat{w}[k]|^2}{|\hat{w}[k]|^2 + \lambda_w}\right)^2} \tag{36}$$

where $\mathbf{w}_{\lambda_w}$ is the solution of (18) to a specific regularization parameter λ_w. The $\alpha,\ \beta > 0$ are the split Bregman tradeoff parameters. We find that the recommended values of $\alpha = 0.5$, $\beta = 1$ from Gholami and Sacchi [2] work well for GPR data with Gaussian noise. High values make the numerical problem unstable. Our tests show that in data sets with high-amplitude low-frequency noise (typical for some GPR data) $\alpha = 0.001 - 0.01$, $\beta = 1$ produce optimal reflectivity and wavelet models.

IV. Numerical Results

Synthetic data sets with two different noise levels and a field data set incorporating cylindrical objects (pipes and tree roots) buried in soil are considered for performance evaluation of the proposed method.

A. Synthetic Data, Cylindrical Objects Model, and Low Noise Level

The first model uses a mixed-phase GPR wavelet with 1-GHz (Hertzian dipole antenna with a transmitter–receiver offset of 3 cm) system response over three cylinders with different sizes and depths embedded in a homogeneous soil (see Table I for details). Cylinders have higher velocities than the background soil. Synthetic data are created with the software package gprMax [45] in 3-D. Noise is added to the modeled data, with a Gaussian distribution of high-frequency noise centered at 1.2 GHz and the peak value of 15% of the pulse amplitude, and lower frequency noise (500 MHz) added at a lower level (10% of pulse amplitude) (Fig. 1). To avoid the complexity of the direct wave, we applied a background removal filter to mute the direct wave. To estimate the initial wavelet, five traces around the apex of each hyperbolic event (seen in black boxes in Fig. 1) are selected, time-shifted to maximize zero-lag cross correlation, stacked and finally normalized [Fig. 2 (top)].

After seven iterations of the main loop of the algorithm, the model converges to the desired minimum, resulting in a final wavelet [red dashed line in Fig. 2 (top)] very close to the true wavelet [black line in Fig. 2 (top)] and a favorable sparse estimate of the reflectivity model [Fig. 2 (bottom)].

TABLE I

Object and Soil Characteristics for Synthetic Data Shown in Fig. 1. Information About the Antenna and Split Bregman Parameters Is Included in the Bottom Half

Object	Depth (cm)	Diameter (cm)	Relative Permittivity
Left	19	2	7
Middle	21	6	8
Right	17	4	10
Soil			5
Antenna Frequency (GHz)	**Time Window (ns)**	**α**	**β**
1	7	0.5 for case 1 and 0.001 for case 2	1 for case 1 and 0.5 for case 2

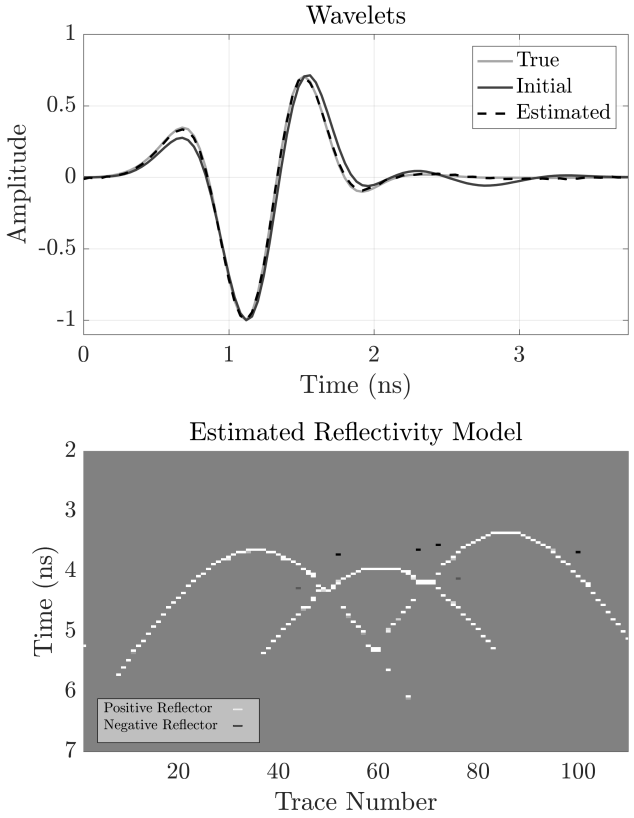

Fig. 2. Results from the deconvolution of the synthetic data shown in Fig. 1. (Top) True synthetic, initial, and final estimated wavelets. The graph shows the full length (3.7 ns) of the assumed wavelet. (Bottom) Estimated reflectivity model.

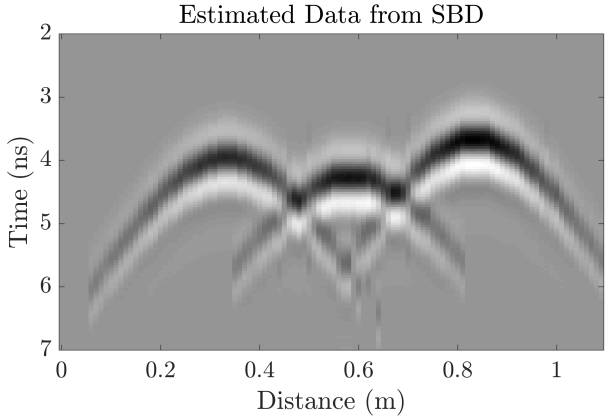

Fig. 3. Estimated data from SBD for the cylinders model with high-frequency noise and moderate low-frequency noise. Comparison with Fig. 1 shows the noise is reduced.

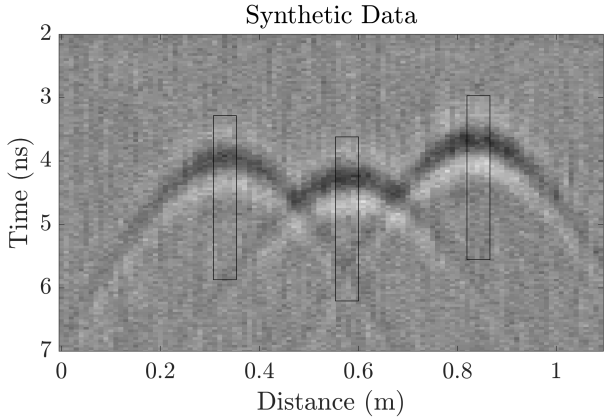

Fig. 4. Synthetic 1-GHz 3-D GPR model over buried cylinders as given in Fig. 1, but with higher levels of low-frequency noise. Black boxes indicate trace segments used for initial wavelet estimation. Early direct wave arrivals are removed before analysis.

The polarity, location, and shape of the hyperbolic returns from the cylinders are extremely well recovered. The low-frequency random noise triggers very few sparse isolated reflectors. The data estimated from the convolution product of the final wavelet and the reflectivity model are shown in Fig. 3. Comparing this result with the original data in Fig. 1 shows the proposed SBD algorithm is an efficient method for reducing the level of high-frequency noise. It should also be noted that a higher resolution image of the estimated reflectivity models is obtained after SBD compared to the collected data as the impact of the transmitted pulse is erased from the data. The estimated reflectivity model is an ideal model that can be used in traditional curve fitting to identify the geometry and location of the reflecting objects.

B. Synthetic Data, Cylindrical Objects Model, and High Noise Level

To create a somewhat more realistic case, a higher level of low-frequency noise (30% of pulse amplitude with 100–600-MHz frequency range) is added to the previously described model (Fig. 4). Such low-frequency noise, typical of many GPR data sets, is much more challenging to remove than high-frequency noise. We find that with the selection of

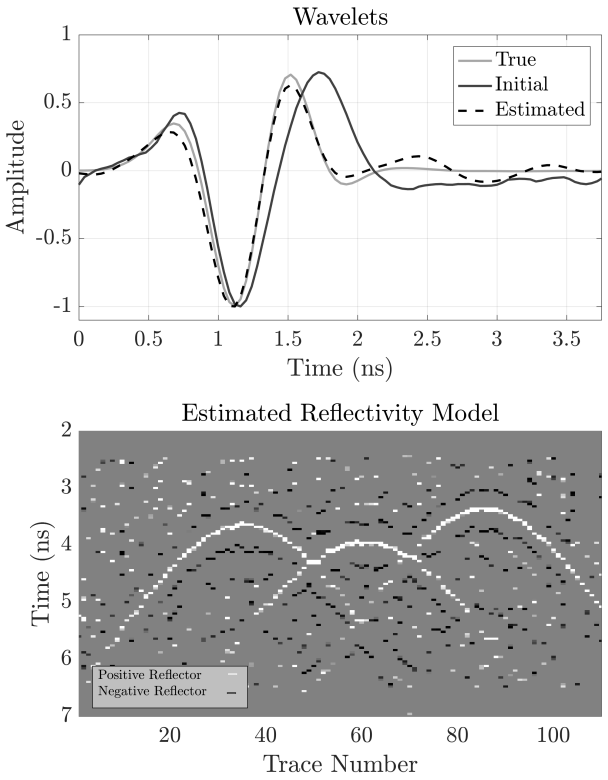

Fig. 5. Results from the deconvolution of the noisier synthetic data shown in Fig. 4. (Top) True, initial, and final estimated wavelets using the same split Bregman parameters $\alpha = 0.5$ and $\beta = 1$, which were used in the lower noise case in Fig. 2. (Bottom) Estimated reflectivity model of the cylinders. Random spikes caused by the low-frequency noise could make it challenging to identify the hyperbolic reflector.

$\alpha = 0.5$ and $\beta = 1$, the SBD fails to remove much of the noise and the reconstructed reflectivity model clearly suffers (Fig. 5). Here, the location and the shape of the hyperbolic reflectors are well recovered, but the reflectivity model could be difficult to interpret against the background noise. The estimated wavelet also suffers from the noise, especially at the tail of the pulse, where the amplitude fails to converge rapidly to zero (orange dashed pulse in Fig. 5).

To do a better job at reducing the low-frequency noise, a range of the split Bregman tradeoff parameters were tested. We find that for GPR data with high levels of low-frequency noise, $\alpha = 0.01$ to 0.001 and $\beta = 0.5$ are more successful in noise reduction and optimal reflectivity and wavelet recovery. Fig. 6 is obtained with $\alpha = 0.001$ and $\beta = 0.5$ ($\alpha = 0.01$ produces almost the same results). Comparison of Figs. 5 and 6 clearly illustrates the importance of the selection of the split Bregman tradeoff parameters. The shape of the estimated wavelet in both cases is generally similar, but the estimated source wavelet in Fig. 6 is much closer to the true wavelet, especially in the tail. Some sparse random reflectors remain in the model, presumably due to the similarity between the noise and the pulse frequencies at those locations.

C. Real Data

A Mala ProEX system with an 800-MHz shielded antenna pair was used to gather a common-offset profile over an 8-cm-diameter metallic pipe buried in the sand (at distance

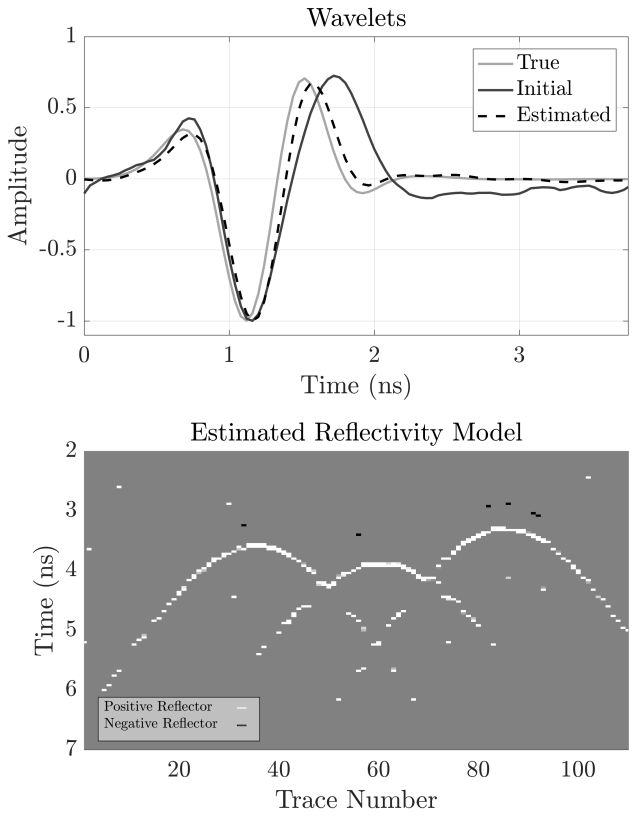

Fig. 6. (Top) True, initial, and estimated wavelets as given in Fig. 5, but with split Bregman tradeoff parameters $\alpha = 0.001$ and $\beta = 0.5$. (Bottom) Estimated reflectivity model of the cylinders is much less noisy, compared to Fig. 5.

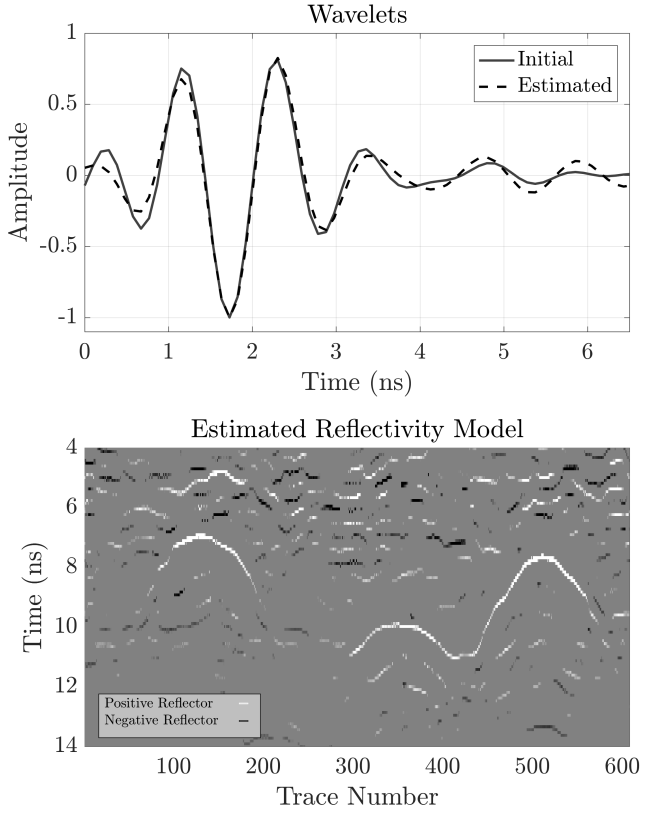

Fig. 8. (Top) Initial and final estimated wavelets for the data set shown in Fig. 7 with $\alpha = 0.5$ and $\beta = 1$. (Bottom) Corresponding estimated reflectivity model. The reflectivity image contains more complexity than desired.

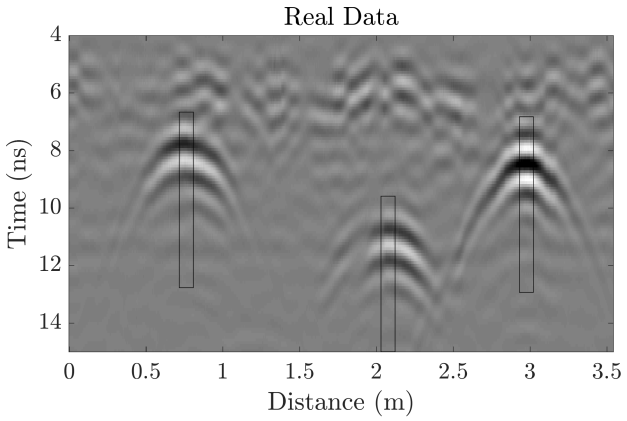

Fig. 7. GPR transect over a metallic pipe (0.75 m along profile) and tree roots (2.1 and 3.0 m) in sand. A low-pass (2 GHz) filter has been applied to reduce high-frequency noise. The direct wave arrival has been cropped from the top of the time axis. No gains are applied. Black boxes contain trace segments used in the initial wavelet calculation.

approximately 0.75 m along the GPR profile shown in Fig. 7). Two other distinctive hyperbolic patterns are seen in the data; these are created by tree roots. High-frequency noise is removed from the data by a simple low-pass filter removing frequencies greater than 2 GHz. Soil heterogeneities generate additional radar returns, especially visible around 6-ns two-way travel time.

Similar to the synthetic models, a background removal is applied and the computation of the initial wavelet does not use the direct wave (before 4 ns, not shown). This is because the direct wave varies along the transect due to variations in soil moisture, surface roughness, and antenna-ground coupling (Fig. 7). This first arrival also falls in the near field of the antenna, and compensation for near-field effects is beyond the scope of this paper (in such settings, it would likely be more effective to estimate the optimum wavelet and reflectivities for each individual transmitter location separately, rather than estimating one best-fit wavelet for the whole data set, a topic also beyond the scope of this paper).

The initial wavelet is calculated by time shifting, stacking, and finally normalizing a few traces around the apex of each hyperbolic event shown in boxes in Fig. 7 (similar to the synthetic case). As for the "noisier" synthetic case, selection of the split Bregman parameters strongly influences results. Comparing Figs. 8 and 9, setting $\alpha = 0.001$ and $\beta = 0.5$ reduces the number of estimated reflectors ($\alpha = 0.01$ provided almost the same reflectivity and wavelet model as $\alpha = 0.001$.) In this latter case (Fig. 9), the hyperbolic shapes of the pipe and roots reflectors are recovered well with fewer reflectors placed earlier than 6 ns and later than the hyperbola arrivals. We stress that in this particular case, recovering the reflectivity model of cylindrical objects was the desired target, rather than soil heterogeneity. The overall shape of the source wavelet recovered with both parameter selections is similar (Figs. 8 and 9), but the latter model yields fewer noncylindrical target reflectors. We find that limiting the source wavelet length to just

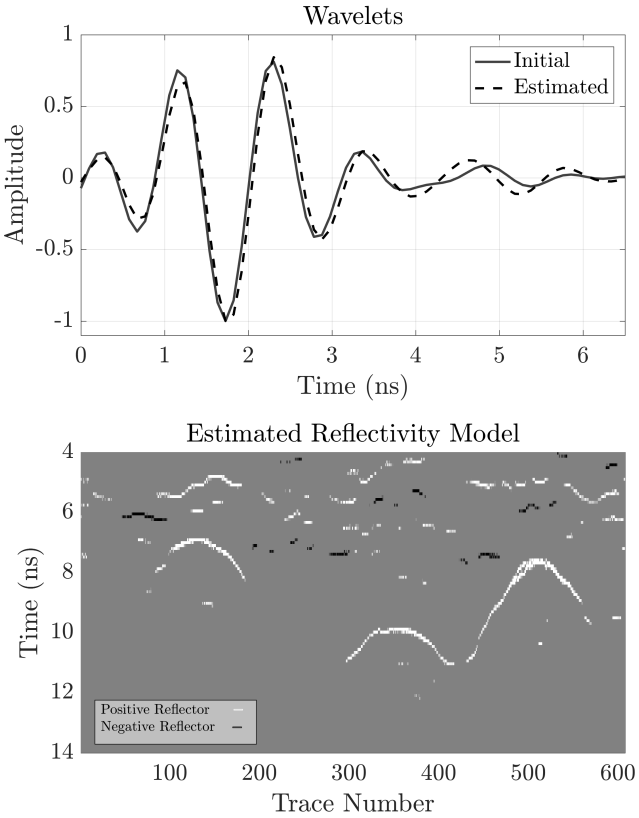

Fig. 9. (Top) Initial and final estimated wavelets for the data set shown in Fig. 7 with $\alpha = 0.001$ and $\beta = 0.5$ ($\alpha = 0.01$ provides very similar models). (Bottom) Corresponding estimated reflectivity model. The additional peak in the early part of the wavelet allows parts of the complexity in the data to be shifted from the reflectivity series to the wavelet.

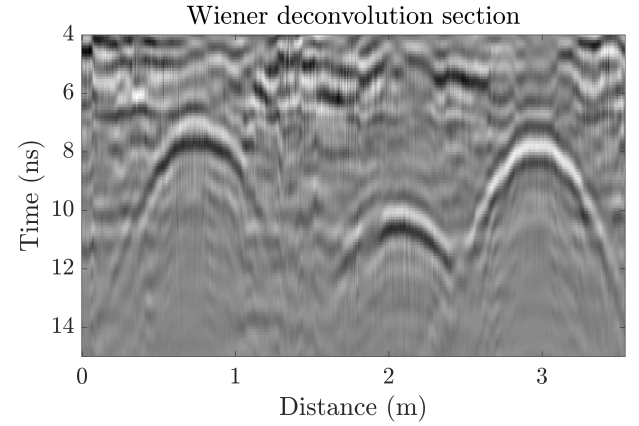

Fig. 10. Wiener deconvolution reflectivity series for the real data in Fig. 7. The signature of the source wavelet is reduced but the reflectivity series still shows the residual wavelet, i.e., the difference between the actual wavelet and its minimum phase equivalent.

the main cycle (i.e., <4 ns length) generates an undesirable train of hyperbolas in the estimated reflectivity model.

Finally, we compare the performance of the SBD algorithm (Fig. 9) with Wiener deconvolution (Fig. 10). Wiener deconvolution assumes that the wavelet has minimum phase and that the reflectivity series is white noise. These assumptions are not satisfied in real-world GPR data, and as a result, the Wiener deconvolution is less effective at removing the effect of the wavelet from the data. Although the recovered reflectivity series (Fig. 10) shows more focused events than the original data (Fig. 7), the series is smooth and lacks the high-resolution features present in the SBD reflectivity series (Fig. 9).

V. Conclusion

The proposed SBD method is tested on synthetic and simple field GPR data. The method estimates the reflectivity model of the subsurface and the transmitted pulse shape efficiently and simultaneously without requiring any prior information from the subsurface or any assumption about the phase of the wavelet. The initial source wavelet estimate is made by extracting and averaging a subset of the data. The process then iteratively updates the reflectivity model and source wavelet. The method is tested on data sets with cylindrical targets and different noise levels. High-frequency noise alone is handled with the split Bregman algorithm parameters $\alpha = 0.5$ and $\beta = 1$, while scenarios with more low-frequency noise and a complex pulse are better treated with $\alpha = 0.01$ to 0.001 and $\beta = 0.5$. The hyperbolic shapes of the recorded signals are well recovered in the reflectivity models. In the synthetic models, the initial wavelet estimate is improved upon, and the final wavelet estimate is a good fit to the true wavelet.

For GPR studies, SBD can be useful for image resolution enhancement and better understanding of the source wavelet. Both the estimated source wavelet and reflectivity model can be used in further advanced modeling procedures such as FWI. Compensation for near-field signal propagation effects is a subject of future research.

Acknowledgment

The authors would like to thank S. Esmaeili for assistance in making plots, and A. Ebrahimi for guidance and constructive discussions. They would also like to thank three anonymous reviewers and the associate editor who gave constructive reviews that greatly improved this paper.

References

[1] F. Sroubek and P. Milanfar, "Robust multichannel blind deconvolution via fast alternating minimization," *IEEE Trans. Image Process.*, vol. 21, no. 4, pp. 1687–1700, Apr. 2012.

[2] A. Gholami and M. D. Sacchi, "A fast and automatic sparse deconvolution in the presence of outliers," *IEEE Trans. Geosci. Remote Sens.*, vol. 50, no. 10, pp. 4105–4116, Oct. 2012.

[3] G. P. Angeleri, "A statistical approach to the extraction of the seismic propagating wavelet," *Geophys. Prospecting*, vol. 31, no. 5, pp. 726–747, 1983.

[4] R. E. Sheriff and L. P. Geldart, *Exploration Seismology*. Cambridge, U.K.: Cambridge Univ. Press, 1995.

[5] J. Xia, E. K. Franseen, R. D. Miller, T. V. Weis, and A. P. Byrnes, "Improving ground-penetrating radar data in sedimentary rocks using deterministic deconvolution," *J. Appl. Geophys.*, vol. 54, nos. 1–2, pp. 15–33, 2003.

[6] N. Economou, A. Vafidis, H. Hamdan, G. Kritikakis, N. Andronikidis, and K. Dimitriadis, "Time-varying deconvolution of GPR data in civil engineering," *Nondestruct. Test. Eval.*, vol. 27, no. 3, pp. 285–292, 2012.

[7] N. Economou and A. Vafidis, "GPR data time varying deconvolution by kurtosis maximization," *J. Appl. Geophys.*, vol. 81, pp. 117–121, Jun. 2012.

[8] I. Abdel-Qader, V. Krause, F. Abu-Amara, and O. Abudayyeh, "Comparative study of deconvolution algorithms for GPR bridge deck imaging," *WSEAS Trans. Signal Process.*, vol. 10, no. 1, pp. 9–20, 2014.

[9] V. Krause, "Blind source separation for feature detection and segmentation in ground penetrating radar (GPR) lmaging of concrete bridge decks for nondestructive condition assessment," Dept. Elect. Comput. Eng., Western Michigan Univ., Kalamazoo, MI, USA, 2015.

[10] C. Schmelzbach and E. Huber, "Efficient deconvolution of ground-penetrating radar data," *IEEE Trans. Geosci. Remote Sens.*, vol. 53, no. 9, pp. 5209–5217, Sep. 2015.

[11] S. Zhao, P. Shangguan, and I. L. Al-Qadi, "Application of regularized deconvolution technique for predicting pavement thin layer thicknesses from ground penetrating radar data," *NDT E Int.*, vol. 73, pp. 1–7, Jul. 2015.

[12] D. Arosio, "Rock fracture characterization with GPR by means of deterministic deconvolution," *J. Appl. Geophys.*, vol. 126, pp. 27–34, Mar. 2016.

[13] J. Xiao and L. Liu, "Permafrost subgrade condition assessment using extrapolation by deterministic deconvolution on multifrequency GPR data acquired along the Qinghai-Tibet railway," *IEEE J. Sel. Topics Appl. Earth Observ. Remote Sens.*, vol. 9, no. 1, pp. 83–90, Jan. 2016.

[14] J. R. Ernst, A. G. Green, H. Maurer, and K. Holliger, "Application of a new 2D time-domain full-waveform inversion scheme to crosshole radar data," *Geophysics*, vol. 72, no. 5, pp. J53–J64, 2007.

[15] A. Klotzsche, J. van der Kruk, G. A. Meles, J. Doetsch, H. Maurer, and N. Linde, "Full-waveform inversion of cross-hole ground-penetrating radar data to characterize a gravel aquifer close to the Thur River, Switzerland," *Near Surf. Geophys.*, vol. 8, no. 6, pp. 635–649, 2010.

[16] S. Jazayeri, A. Klotzsche, and S. Kruse, "Improving estimates of buried pipe diameter and infilling material from ground-penetrating radar profiles with full-waveform inversion," *Geophysics*, vol. 83, no. 4, pp. H27–H41, 2018, doi: 10.1190/geo2017-0617.1.

[17] N. Levinson, "The Wiener (root mean square) error criterion in filter design and prediction," *Stud. Appl. Math.*, vol. 25, nos. 1–4, pp. 261–278, Apr. 1946.

[18] E. A. Robinson, "Predictive decomposition of seismic traces," *Geophysics*, vol. 22, no. 4, pp. 767–778, 1957.

[19] N. Ricker, "The form and laws of propagation of seismic wavelets," *Geophysics*, vol. 18, no. 1, pp. 10–40, 1953.

[20] R. A. Wiggins, "Minimum entropy deconvolution," *Geoexploration*, vol. 16, nos. 1–2, pp. 21–35, 1978.

[21] M. D. Sacchi and T. J. Ulrych, "Nonminimum-phase wavelet estimation using higher order statistics," *Lead. Edge*, vol. 19, no. 1, pp. 80–83, 2000.

[22] K. F. Kaaresen and T. Taxt, "Multichannel blind deconvolution of seismic signals," *Geophysics*, vol. 63, no. 6, pp. 2093–2107, 1998.

[23] N. Kazemi and M. D. Sacchi, "Sparse multichannel blind deconvolution," *Geophysics*, vol. 79, no. 5, pp. V143–V152, 2014.

[24] N. Kazemi, E. Bongajum, and M. D. Sacchi, "Surface-consistent sparse multichannel blind deconvolution of seismic signals," *IEEE Trans. Geosci. Remote Sens.*, vol. 54, no. 6, pp. 3200–3207, Jun. 2016.

[25] N. Kazemi, "Blind deconvolution with Toeplitz-structured sparse total least squares algorithm," in *Proc. 80th EAGE Conf. Exhib.*, 2018, doi: 10.3997/2214-4609.201800882.

[26] K. Chahine, V. Baltazart, Y. Wang, and X. Dérobert, "Blind deconvolution via sparsity maximization applied to GPR data," *Eur. J. Environ. Civil Eng.*, vol. 15, no. 4, pp. 575–586, 2011.

[27] L. Li, "Sparsity-promoted blind deconvolution of ground-penetrating radar (GPR) data," *IEEE Geosci. Remote Sens. Lett.*, vol. 11, no. 8, pp. 1330–1334, Aug. 2014.

[28] E. A. Robinson and S. Treitel, *Geophysical Signal Analysis*, vol. 263. Upper Saddle River, NJ, USA: Prentice-Hall, 1980.

[29] A. Osen, B. G. Secrest, L. Amundsen, and A. Reitan, "Wavelet estimation from marine pressure measurements," *Geophysics*, vol. 63, no. 6, pp. 2108–2119, 1998.

[30] R. L. Brown, W. McElhattan, and D. J. Santiago, "Wavelet estimation: An interpretive approach," *Lead. Edge*, vol. 7, no. 12, pp. 16–19, 1988.

[31] E. Bianco, "Geophysical tutorial: Well-tie calculus," *Lead. Edge*, vol. 33, no. 6, pp. 674–677, 2014.

[32] O. Shalvi and E. Weinstein, "New criteria for blind deconvolution of nonminimum phase systems (channels)," *IEEE Trans. Inf. Theory*, vol. 36, no. 2, pp. 312–321, Mar. 1990.

[33] D. R. Velis, "Stochastic sparse-spike deconvolution," *Geophysics*, vol. 73, no. 1, pp. R1–R9, 2007.

[34] H. W. J. Debeye and V. P. Riel, "L_p-norm deconvolution," *Geophys. Prospecting*, vol. 38, no. 4, pp. 381–403, 1990.

[35] J.-L. Starck, F. Murtagh, and J. M. Fadili, *Sparse Image and Signal Processing: Wavelets, Curvelets, Morphological Diversity*. Cambridge, U.K.: Cambridge Univ. Press, 2010.

[36] A. Repetti, M. Pham, L. Duval, E. Chouzenoux, and J.-C. Pesquet, "Euclid in a taxicab: Sparse blind deconvolution with smoothed ℓ_1/ℓ_2 regularization," *IEEE Signal Process. Lett.*, vol. 22, no. 5, pp. 539–543, May 2015.

[37] I. Selesnick, "Sparse deconvolution (an MM algorithm)," *Connexions*, 2012. [Online]. Available: https://goo.gl/mGDx7m

[38] M. A. T. Figueiredo, R. D. Nowak, and S. J. Wright, "Gradient projection for sparse reconstruction: Application to compressed sensing and other inverse problems," *IEEE J. Sel. Topics Signal Process.*, vol. 1, no. 4, pp. 586–597, Dec. 2007.

[39] T. Goldstein and S. Osher, "The split Bregman method for L1-regularized problems," *SIAM J. Imag. Sci.*, vol. 2, no. 2, pp. 323–343, 2009.

[40] G. Hennenfent, E. van den Berg, M. P. Friedlander, and F. J. Herrmann, "New insights into one-norm solvers from the Pareto curve," *Geophysics*, vol. 73, no. 4, pp. A23–A26, 2008.

[41] D. O. Pérez, D. R. Velis, and M. D. Sacchi, "High-resolution prestack seismic inversion using a hybrid FISTA least-squares strategy," *Geophysics*, vol. 78, no. 5, pp. R185–R195, 2013.

[42] G. Wahba, "The approximate solution of linear operator equations when the data are noisy," *Adv. Appl. Probab.*, vol. 8, no. 2, pp. 222–223, 1976.

[43] D. J. Cummins, T. G. Filloon, and D. Nychka, "Confidence intervals for nonparametric curve estimates: Toward more uniform pointwise coverage," *J. Amer. Stat. Assoc.*, vol. 96, no. 453, pp. 233–246, 2001.

[44] A. Ebrahimi, A. Gholami, and M. Nabi-Bidhendi, "Sparsity-based GPR blind deconvolution and wavelet estimation," *J. Ind. Geophys. Union*, vol. 21, no. 1, pp. 7–12, 2017.

[45] C. Warren, A. Giannopoulos, and I. Giannakis, "gprMax: Open source software to simulate electromagnetic wave propagation for ground penetrating radar," *Comput. Phys. Commun.*, vol. 209, pp. 163–170, Dec. 2016.

Sajad Jazayeri received the B.Sc. degree in physics from Razi University, Kermanshah, Iran, in 2007, and the M.Sc. degree in geophysics from the University of Tehran, Tehran, Iran, in 2009. He is currently pursuing the Ph.D. degree with the Geophysics Group, University of South Florida, Tampa, FL, USA.

Since 2014, he has been with the School of Geosciences, University of South Florida. His research interests include full-waveform inversion, and modeling and imaging of geophysical data.

Nasser Kazemi received the B.Sc. degree in geology from the University of Tabriz, Tabriz, Iran, in 2007, the M.Sc. degree in geophysics from the University of Tehran, Tehran, Iran, in 2010, and the Ph.D. degree in geophysics from the University of Alberta, Edmonton, AB, Canada, in 2017.

From 2012 to 2017, he was with the Signal Analysis and Imaging Group, University of Alberta, where he was involved in seismic depth imaging and seismic signal processing. He also briefly collaborated with the Statoil ASA Research Group, Trondheim, Norway, in 2014. In 2017, he joined the University of Calgary, Calgary, AB, Canada, as a Post-Doctoral Associate Researcher. He is the point person for integrating seismic and seismic-while-drilling imaging with the development and production workflows. His research interests include the signal analysis and seismic imaging.

Dr. Kazemi was a recipient of Canada First Research Excellence Fund Fellowship, University of Calgary.

Sarah Kruse is currently a Professor with the School of Geosciences, University of South Florida, Tampa, FL, USA. He is involved in ground penetrating radar applied to void detection, sinkhole hazards, and engineering targets. Her research interests include near-surface geophysics.